Box Spline Wavelet Frames for Image Edge Analysis[*]

Weihong Guo[†] and Ming-Jun Lai[‡]

Abstract. We present a new box spline wavelet frame and apply it for image edge analysis. The wavelet frame is constructed using a box spline of eight directions. It is tight and has seldom been used for applications. Due to the eight different directions, it can find edges of various types in detail quite well. In addition to step edges (local discontinuities in intensity), it is able to locate Dirac edges (momentary changes of intensity) and hidden edges (local discontinuity in intensity derivatives). The method is simple and robust to noise. Many numerical examples are presented to demonstrate the effectiveness of this method. Quantitative and qualitative comparisons with other edge detection techniques are provided to show the advantages of this wavelet frame. Our test images include synthetic images with known ground truth and natural, medical images with rich geometric information.

1. Introduction. Edge detection is consistent with human perception and is usually the first step in image interpretation and understanding. Edges provide the topology and structural information of essential objects in an image. In other words, edges present the skeleton of an image. Edge information can be used directly for feature extraction, object identification, region segmentation, etc. It can also be used as a priori information to help improve other tasks such as image denoising, image restoration, image reconstruction, and pattern recognition. The general edge detection task recovers step edges (local discontinuities in intensity), Dirac edges (momentary changes of intensity), and other edges such as hidden edges (discontinuous locations of some directional derivatives of images). Certainly, edge detectors produce edges with some compromise among accuracy, completeness, and smoothness. The goal of this research is to find the details of an image as accurately as possible.

In this paper, we present an edge detector based on box spline wavelet frames. We show that it is able to detect edges very well. An advantage of frames is that they consist of many redundant functions which can approximate various edges and features better than linearly independent functions. Box splines are compactly supported piecewise polynomial functions. They are smooth and refinable and hence are often used to construct various wavelet functions such as biorthogonal wavelets, prewavelets, and tight wavelet frames in the multivariate setting (cf. [19, 24, 28] for their explicit formulas with any degrees of regularity). Although it has been known for several years that wavelet functions can be used for image edge detection, the

---

[†]Department of Mathematics, Case Western Reserve University, Cleveland, OH, 44106 (wxg49@case.edu). The first author is partially supported by NIH grant 1R21EB016535-01.

[‡]Department of Mathematics, The University of Georgia, Athens, GA 30602 (mjlai@math.uga.edu).

performance and effectiveness of box spline wavelet frames for such applications are not well understood. In particular, it is not known which box spline wavelet frame works best for edge extraction. Following the construction method in [28] and the work [34], we have obtained box spline wavelet framelets based on various box splines, $B_{111}, B_{221}, B_{222}, B_{1111}, B_{2111}, B_{2211}$, on a three and a four direction mesh (cf. [13] or [27]), and B_8, which is a box spline based on eight different directions to be explained in section 3.

We have tested these wavelet frames as well as those based on the tensor product of univariate linear, quadratic, cubic, and quadratic B-splines for edge detection on various images. The experiments show that B_8 is most effective in catching the details of images. Qualitative and quantitative comparisons with some other types of edge detectors, such as Canny, Prewitt, and shearlet based methods, show that the proposed box spline edge detector produces more accurate edges under similar conditions. For the sake of fair comparison, we start with a synthetic image with ground truth edges and apply four edge detectors under various parameter settings to this image. We then compare the best results of the four methods using *Pratt's figure of merit* (Figure 2) and compare results under various parameter settings using *probability of detection* (Figure 3). These comparison results show that the proposed edge detector leads to a higher figure of merit and consistently higher probability of detection. Visual qualitative comparisons on other natural images (Figures 4–10) imply that the proposed edge detector is able to catch fine details and is robust to noise. We explain the details in section 3 and demonstrate the results in section 4 with various applications.

The paper is organized as follows: we start with a literature review of some edge detection methods in section 2. Section 3 discusses the construction of box spline wavelet frames and how to use them to remove noise and to detect edges. In particular, we introduce a new box spline function based on an eight direction mesh and use it to construct wavelet frames. In section 4, we compare the proposed box spline edge detector with several others and demonstrate that the proposed approach always performs best in capturing the details of images. In addition, we present examples to find hidden edges of images in section 4.4. Finally, conclusions are drawn in section 5.

2. Review of edge detectors. In this section we review some existing edge detectors.

2.1. Partial derivative based edge detectors. An important class of existing edge detectors is based on partial derivatives of the input image. Image pixels with maximum gradients or zero Laplacians are classified as edges [3, 14, 20, 29, 32, 21]. These gradient based edge detectors typically include three steps. First, noise is reduced if the input image is noisy; usually a Gaussian convolution is applied. Second, the partial derivatives are estimated by convolving with some kernels. Various kernels have been developed for this purpose with different accuracies along different directions (cf. [49, 47]). Prewitt and Canny edge detectors, for instance, differ only in the kernels used to approximate the partial derivatives. Third, edges are located where the norms of the gradients are above a threshold. Standard thresholding techniques treat pixels with gradient magnitude greater than a threshold as edges. Hysteresis thresholding uses two different thresholds. Any pixel with gradient magnitude above the larger threshold is characterized as an edge; so are those pixels that are in the neighborhood of this pixel and with their gradient magnitudes higher than the smaller threshold. This hysteresis thresholding technique leads to connected edges and is sometimes referred to as

linking. Nonmaximum suppression is sometimes used to thin edges in a method such as the Canny method.

Edge detectors of this type are robust to low-level noise, but they tend to mistakenly detect fake edges due to excessive noise/artifacts. To alleviate this issue, one can further incorporate local mutual information (cf., e.g., [17]).

2.2. Continuous wavelet based edge detector and shearlet based edge detector. Mallat's wavelet based method [31] can detect both the location and the types (such as step and Dirac) of edges through analyzing *local Lipschitz regularity*, a quantity related to how fast the wavelet transfrom coefficients change across scales. We first briefly review the definitions of Lipschitz regularity and wavelet transform; then we review a theorem that relates the two of them. Refer to [31] for more details.

Definition 2.1 (Lipschitz regularity). *Let* $0 \leq \alpha \leq 1$. *A function* $f(x)$ *is uniformly Lipschitz* α *over an interval* (a, b) *if there exists a constant* C *such that for any* $x_0, x_1 \in (a, b)$, $|f(x_0) - f(x_1)| \leq C|x_0 - x_1|^{\alpha}$. *The Lipschitz regularity of* $f(x)$ *is defined as the upper bound* α_0 *of all* α *satisfying the above condition.*

The Lipschitz regularity of a function is related to continuity/singularity. For instance, if $f(x)$ is differentiable at x_0, then it is Lipschitz 1 near x_0. Lipschitz regularity is difficult to verify directly, but Mallat and Zhong proposed a theorem to relate the local Lipschitz regularity with the dyadic wavelet transform. Recall that a nonzero function $\omega \in L^1(\mathbb{R})$ is called a wavelet if $\int_{-\infty}^{\infty} \omega(x) dx = 0$ (cf. [11, p. 3]). With a wavelet function, we can define the wavelet transform as follows.

Definition 2.2 (wavelet transform). *Let* ω *be a wavelet function. The continuous wavelet transform of* f *with respect to* ω *at scale* s *is defined as* $W_s f(x) := \int_{-\infty}^{\infty} f(y) \frac{\omega((y-x)/s)}{s} dy$. *For dyadic wavelet transforms, the scale* s *is chosen as* $s = 2^j$ *and* $x = 2^j n$ *for* $j, n \in \mathbb{Z}$.

A wavelet transform can be used to characterize local regularities of functions. See Theorem 1 in [31] and/or Theorems 2.91–2.92 in [11] for a proof of the following theorem.

Theorem 2.3. *Let* $0 < \alpha \leq 1$. *A function* $f(x)$ *is uniformly Lipschitz* α *over* (a, b) *if and only if there exists a constant* $K > 0$ *such that the wavelet transform satisfies* $|W_{2^j} f(x)| \leq K(2^j)^{\alpha}$ *for all* $x \in (a, b)$ *and* $j = 1, 2, \ldots$.

According to this theorem, if a function f has a Lipschitz regularity for $0 < \alpha \leq 1$, the value of $\sup_{x \in (a,b)} |W_{2^j} f(x)|$ should decrease as the scale j decreases. If $\sup_{x \in (a,b)} |W_{2^j} f(x)|$ increases instead, then f does not have a Lipschitz regularity and thus must have an impulse (Dirac) at x. If $\sup_{x \in (a,b)} |W_{2^j} f(x)|$ does not change much across the scales, it indicates that $\alpha = 0$ and there is a jump at x. These facts form a basis for using a wavelet transform to detect edges.

On the other hand, it is known that a continuous wavelet based edge detector has difficulty in distinguishing nearby edges and has a poor angular accuracy (cf. [31]). This is due to the well-known fact that wavelets are perfect in describing *isotropic* structures but not so good dealing with *anisotropic* phenomena. More recently, shearlets [15, 22] have been used for edge detection and analysis (cf. [46]). It is claimed that shearlets are effective in detecting the location and orientation of edges as well as the number of edges at each point. A shearlet transform decomposes an image with respect to scale, location, and orientation. The orientation information at each scale is directly available. The locations of image edges are then

determined by the changes in shearlet transform coefficients across scales. The orientations of edges are extracted from the directions in which the shearlet transform coefficients are significant, while the number of edges at each point is determined by the number of peaks of the shearlet transform coefficients.

2.3. Segmentation based edge detectors. Although image segmentation is different from edge detection, they are related, and one can also extract edges from the segmentation results. Image segmentation [33, 2, 4] partitions the image domain into different subregions that are each homogeneous with respect to some characteristics such as intensity. The borders of those subregions form the edges. To give more mathematical details, we take the two-phase Mumford–Shah method as an example. Let g be the intensity function of an input image. The method separates the image domain into two parts Ω_1 and Ω_2, one inside the edge contour Γ and the other outside, such that g can be approximated by C^1 functions f_1, f_2 in Ω_1, Ω_2, respectively. The separation is done by minimizing the functional

$$E(f_1, f_2, \Gamma) = \frac{1}{2} \int_{\Omega_1} (g - f_1)^2 + \frac{1}{2} \int_{\Omega_2} (g - f_2)^2 + \alpha \int_{\Omega_1} |\nabla f_1|^2 + \alpha \int_{\Omega_2} |\nabla f_2|^2 + \beta \cdot \mathrm{Length}(\Gamma)$$

with respect to functions f_1, f_2 and contour Γ. In the special case where f_1, f_2 are constant with values c_1, c_2, respectively, the implementation of the Mumford–Shah model is simplified by the Chan–Vese method [4] based on the level set approach (cf. [35]). It represents the edge contour Γ by the zero level set of a Lipschitz function $\Phi : \Omega \to \mathbb{R}$ and the regions inside and outside the contour Γ by the regions with positive and negative Φ values, respectively. Let $H(\cdot)$ be the Heaviside function defined as $H(z) = 1$ for positive z and 0 elsewhere. Then the minimizer Φ of

$$\frac{1}{2} \int_{\Omega} [H(\Phi)(g - c_1)^2 + (1 - H(\Phi))(g - c_2)^2] + \beta \int_{\Omega} |\nabla H(\Phi)|$$

gives the segmentation of the domain and the edge contours. The edges are detected from the 0 level set of Φ.

2.4. Other methods. Other edge detection approaches include the Mumford–Shah Green function [30], morphological gradient [41, 36, 38], fractal geometry [48, 44], and high-order and variable-order total variation [42] based methods.

3. Box spline tight wavelet frames. Tight wavelet frames are the generalizations of discrete orthonormal wavelets [39, 40, 9, 10, 12, 34, 28, 26]. An advantage of using frames is that frames consist of many redundant functions which can approximate various edges and features better than using only linearly independent functions. Box splines are refinable functions, and one can easily choose various directions to obtain a box spline function with a desired order of smoothness (see [13], Chapter 12 of [27], [23]). They have been used to construct various wavelet functions including tight wavelet frames. In this section, we first review general box spline tight wavelet frames and then present our derivation of a new box spline wavelet frame based on B_8.

3.1. Review of general box spline tight wavelet frames. We begin with the definition of tight wavelet frames based on a multiresolution approximation of $L_2(\mathbb{R}^2)$. Given a function $\psi \in L_2(\mathbb{R}^2)$, we define

$$\psi_{j,k}(y) = 2^j \psi(2^j y - k)$$

with $k \in \mathbb{Z}^2$ a translation and $j \in \mathbb{Z}$ a dilation. Let Ψ be a finite subset of $L_2(\mathbb{R}^2)$, and let $\Lambda(\Psi) := \{\psi_{j,k}, \psi \in \Psi, j \in Z, k \in Z^2\}$.

Definition 3.1. *We say that* $\Lambda(\Psi)$ *is a* frame *if there exist two positive numbers A and B such that*

$$A\|f\|^2_{L_2(\mathbb{R}^2)} \leq \sum_{g \in \Lambda(\Psi)} |\langle f, g \rangle|^2 \leq B\|f\|^2_{L_2(\mathbb{R}^2)}$$

for all $f \in L_2(\mathbb{R}^2)$. $\Lambda(\Psi)$ *is a* tight frame *if it is a frame with $A = B$. In this case, after a renormalization of the g's in Ψ, we have*

$$\sum_{g \in \Lambda(\Psi)} |\langle f, g \rangle|^2 = \|f\|^2_{L_2(\mathbb{R}^2)}$$

for all $f \in L_2(\mathbb{R}^2)$.

It is known by the polarization identity (cf. [11, p. 101]) that when $\Lambda(\Psi)$ is a tight frame, any $f \in L_2(\mathbb{R}^2)$ can be represented by $g \in \Lambda(\Psi)$ in the following format:

$$f = \sum_{g \in \Lambda(\Psi)} \langle f, g \rangle g \quad \forall f \in L_2(\mathbb{R}^2).$$

Let $\phi \in L_2(\mathbb{R}^2)$ be a compactly supported refinable function; i.e., ϕ satisfies the refinable equation

$$\hat{\phi}(\omega) = P(\omega/2)\hat{\phi}(\omega/2),$$

where $\hat{\phi}$ is the Fourier transform of ϕ and $P(\omega)$ is a Laurent polynomial in $e^{i\omega} = (e^{i\xi}, e^{i\eta})$. P is often called the mask of a refinable function ϕ. We look for another Laurent polynomial Q_i such that

$$(3.1) \qquad P(\omega)\overline{P(\omega + \ell)} + \sum_{i=0}^{r} Q_i(\omega)\overline{Q_i(\omega + \ell)} = \begin{cases} 1 & \text{if } \ell = 0, \\ 0, & \ell \in \{0,1\}^2\pi\backslash\{0\}. \end{cases}$$

The conditions (3.1) are called the *unitary extension principle* (UEP) as in [39, 40, 12]. With these Q_i's we can define wavelet frame generators or framelets $\psi^{(i)}$ in terms of the Fourier transform by

$$(3.2) \qquad \hat{\psi}^{(i)}(\omega) = Q_i(\omega/2)\hat{\phi}(\omega/2), \quad i = 1, \ldots, r.$$

Then, if ϕ has Lipschitz regularity with $\alpha > 0$, $\Psi = \{\psi^{(i)}, i = 1, \ldots, r\}$ generates a tight frame; i.e., $\Lambda(\Psi)$ is a tight wavelet frame (cf. [28]).

Furthermore, assuming $\omega = (\xi, \eta)$, letting $\mathcal{Q}$ be a rectangular matrix defined by

(3.3)
$$\mathcal{Q} = \begin{bmatrix} Q_1(\xi,\eta) & Q_1(\xi+\pi,\eta) & Q_1(\xi,\eta+\pi) & Q_1(\xi+\pi,\eta+\pi) \\ Q_2(\xi,\eta) & Q_2(\xi+\pi,\eta) & Q_2(\xi,\eta+\pi) & Q_2(\xi+\pi,\eta+\pi) \\ Q_3(\xi,\eta) & Q_3(\xi+\pi,\eta) & Q_3(\xi+\pi,\eta) & Q_3(\xi+\pi,\eta+\pi) \\ Q_4(\xi,\eta) & Q_4(\xi+\pi,\eta) & Q_4(\xi+\pi,\eta) & Q_4(\xi+\pi,\eta+\pi) \\ \vdots & \vdots & \vdots & \vdots \\ Q_r(\xi,\eta) & Q_r(\xi+\pi,\eta) & Q_r(\xi+\pi,\eta) & Q_r(\xi+\pi,\eta+\pi) \end{bmatrix},$$

and letting $\mathcal{P} = (P(\xi,\eta), P(\xi+\pi,\eta), P(\xi,\eta+\pi), P(\xi+\pi,\eta+\pi))^\top$, (3.1) is simply

(3.4)
$$\overline{\mathcal{P}}\mathcal{P}^\top + \mathcal{Q}^*\mathcal{Q} = I_{4\times 4},$$

i.e.,

(3.5)
$$\sum_{\ell \in \{0,1\}^2 \pi} |P(\omega + \ell)|^2 = 1.$$

The construction of tight wavelet frames involves finding the $\mathcal{Q}$ that satisfies (3.4), which is called a perfect reconstruction condition. It was observed in [28] that $\mathcal{Q}$ can be easily found if $\mathcal{P}$ satisfies the quadrature mirror filter (QMF) condition $\mathcal{P}^T\mathcal{P} = 1$, i.e., $\sum_{\ell \in \{0,1\}^2 \pi} |P(\omega + \ell)|^2 = 1$. In this case, $\mathcal{Q}$ has a very simple expression. However, the mask P of a refinable function ϕ usually does not satisfy the QMF condition but the following *sub-QMF condition* instead:

(3.6)
$$\sum_{\ell \in \{0,1\}^2 \pi} |P(\omega + \ell)|^2 \leq 1.$$

For example, the masks of bivariate box splines on a three, a four, and an eight direction mesh below satisfy (3.6). Recall that any Laurent polynomial $P(\omega)$ can be rewritten as

$$P(\omega) = P_{(0,0)}(2\omega) + e^{i\xi}P_{(1,0)}(2\omega) + e^{i\eta}P_{(0,1)}(2\omega) + e^{i(\xi+\eta)}P_{(1,1)}(2\omega)$$

for some $P_m, m \in \{0,1\}^2$. These $P_m(\cdot)$ are called polyphases of $P(\cdot)$.

Theorem 3.2 (Lai and Stöckler, 2006). *Suppose that P satisfies the sub-QMF condition* (3.6) *and that there exist Laurent polynomials $\tilde{P}_1, \ldots, \tilde{P}_N$ such that*

(3.7)
$$\sum_{m \in \{0,1\}^2} |P_m(\omega)|^2 + \sum_{i=1}^{N} |\tilde{P}_i(2\omega)|^2 = 1,$$

where $P_m, m \in \{0,1\}^2$, are polyphases of P. Then there exist $4 + N$ compactly supported tight frame generators with wavelet masks $Q_m, m = 1, \ldots, 4+N$, such that $\mathcal{P}, \mathcal{Q}_m, m = 1, \ldots, 4+N$, satisfy (3.4).

Although there is no Riesz–Féjer theorem in the multivariate setting, we are able to find additional Laurent polynomials $\tilde{P}_i$ to satisfy (3.7) for bivariate box spline functions (cf. [28]).

We next recall the definition of bivariate box spline functions on a direction set D. For instance, by letting $e_1 = (1,0), e_2 = (0,1), e_3 = e_1 + e_2, e_4 = e_1 - e_2, e_5 = (2,1), e_6 =$

$(2, -1), e_7 = (1, 2), e_8 = (1, -2)$, one can define D as the set of these vectors with some repetitions. Then the box spline ϕ_D associated with direction set D may be defined in terms of Fourier transform by

$$(3.8) \qquad \hat{\phi}_D(\omega) = P_D\left(\frac{\omega}{2}\right) \hat{\phi}_D\left(\frac{\omega}{2}\right),$$

where P_D is

$$P_D(\omega) = \prod_{\xi \in D} \frac{1 + e^{-i\xi \cdot \omega}}{2}.$$

We refer the interested readers to [7, 13, 27] for many properties of box splines. An explicit polynomial representation of bivariate box splines enables us to evaluate these box splines easily [23, 27]. Note that it is easy to show that the mask P_D satisfies (3.6). To construct the associated tight framelets, we mainly find additional Laurent polynomials to satisfy (3.7). However, it is not an easy task as there is no existence theory or constructive procedure except for box splines on a three and a four direction mesh. This will be further explained in the next subsection.

3.2. The eight direction box spline. When using a box spline wavelet frame, we have the flexibility to choose a direction set. We can choose a box spline function with as many directions as possible to increase the redundancy. However, the more directions there are, the smoother the box spline function will be, and the longer the length of the low pass and high pass filters will be; hence, it will be more difficult to find tiny details in the image. Empirical results show that the wavelet frame based on a box spline with eight directions is the ideal one for edge/feature/detail detection. In this paper we shall present a tight framelet based on box spline $\phi_8 := \phi_{D_8}$ with

$$(3.9) \qquad D_8 = \{e_1, e_2, e_1 + e_2, e_1 - e_2, 2e_1 + e_2, 2e_1 - e_2, e_1 + 2e_2, e_1 - 2e_2\}.$$

Since D_8 contains eight directions, we call ϕ_8 an eight direction box spline. This box spline is new and has not been studied in the literature. It is a bivariate spline function of total degree ≤ 6, which is in C^5. Also ϕ_8 is compactly supported and nonnegative. All the integer translations of ϕ_8 are linearly dependent. Thus they are redundant. But they form a partition of unity after a scale. The mask $P_8 := P_{D_8}$ can be found easily and is

$$(3.10) \qquad \begin{aligned} P_8(\xi, \eta) = &\left(\frac{1 + e^{i\xi}}{2}\right)\left(\frac{1 + e^{i\eta}}{2}\right)\left(\frac{1 + e^{i(\xi+\eta)}}{2}\right)\left(\frac{1 + e^{i(\xi-\eta)}}{2}\right) \\ &\cdot \left(\frac{1 + e^{i(\xi+2\eta)}}{2}\right)\left(\frac{1 + e^{i(2\xi+\eta)}}{2}\right)\left(\frac{1 + e^{i(\xi-2\eta)}}{2}\right)\left(\frac{1 + e^{i(2\xi-\eta)}}{2}\right). \end{aligned}$$

For convenience, we shall write $P_8(\xi, \eta) = \sum_{j,k} p_{j,k} e^{-ij\xi} e^{-ik\eta}$. To use Theorem 3.2, we need to show that (3.7) is satisfied for some $\widetilde{P}_i$. For box splines on a three and a four direction mesh, it is known that the polynomial equation (3.7) has a solution (cf. [28] and [25]). Furthermore, in [16], the researchers showed that (3.7) has a solution in general if the inequality in (3.6)

is strict. The researchers in [6] proposed using semidefinite programming (SDP) to find $\widetilde{P}_1, \ldots, \widetilde{P}_N$ satisfying (3.7). However, SDP is currently only able to solve this problem for small scales.

Recently, the researchers in [5] presented an algebraic approach proving that (3.7) has a solution for box splines on a three and a four direction mesh. For the box spline ϕ_8, it was challenging to solve (3.7) for a number of reasons. First, the number, N, of extra Laurent polynomials $\tilde{P}_j$ is unknown. The degrees of these polynomials are also unknown, although our intuition is that the degrees should be less than or equal to 6, the degree of the 8 direction box spline ϕ_8. We solved (3.7) using brute force. We started with $N = 1$ and used Maple to try to solve (3.7), but it was not successful. We then increased the value of N to 2 and did the same thing. The smallest value for which Maple could find a solution is $N = 10$, which corresponds to a large system of multivariate quadratic equations involving more than 50 variables. We then decoupled these equations and broke the system into smaller subsystems. Eventually, we were able to solve the system within a very small tolerance (e.g., 10^{-10}) and find ten Laurent polynomials $\widetilde{P}_j, j = 1, \ldots, 10$, to satisfy (3.7), i.e.,

$$1 - \sum_{\nu \in \{0,\pi\}^2} |P_8(\omega + \nu)|^2 \approx \sum_{j=1}^{10} |\widetilde{P}_j(2\omega, 2\eta)|^2, \qquad \omega = (\xi, \eta) \in [0, 2\pi]^2.$$

The ten Laurent polynomials are given below:

$$\widetilde{P}_1(\xi, \eta) = \frac{42}{14561} - \frac{542}{4269} e^{i(\xi+4\eta)} + \frac{42}{14561} e^{2i\xi} + \frac{191}{1576} e^{i\xi},$$

$$\widetilde{P}_2(\xi, \eta) = \frac{281}{1476} - \frac{51}{26513} e^{i(4\xi+\eta)} + \frac{281}{1476} e^{2i\eta} - \frac{605}{1597} e^{i(\xi+\eta)},$$

$$\widetilde{P}_3(\xi, \eta) = \frac{1}{192} - \frac{9}{32} e^{i(2\xi+3\eta)} + \frac{1}{192} e^{4i\xi} + \frac{283}{1152} e^{2i(\xi+\eta)} + \frac{29}{1152} e^{2i\xi},$$

$$\widetilde{P}_4(\xi, \eta) = \frac{192}{15731} - \frac{233}{19415} e^{i(3\xi+2\eta)} + \frac{192}{1573} e^{4i\eta} - \frac{172}{741} e^{2i\eta},$$

$$\widetilde{P}_5(\xi, \eta) = \frac{139}{2849} - \frac{278}{2849} e^{i(\xi+3\eta)} + \frac{139}{2849} e^{2i\xi},$$

$$\widetilde{P}_6(\xi, \eta) = \frac{76}{4195} - \frac{843}{3208} e^{i(3\xi+\eta)} + \frac{76}{4195} e^{2i\eta} + \frac{227}{1002} e^{i(\xi+\eta)},$$

$$\widetilde{P}_7(\xi, \eta) = \frac{412}{2807} - \frac{211}{1364} e^{i(\xi+2\eta)} + \frac{412}{2807} e^{2i\xi} - \frac{263}{3788} e^{2i(\xi+\eta)} - \frac{263}{3788} e^{2i\eta},$$

$$\widetilde{P}_8(\xi, \eta) = \frac{152}{2475} - \frac{288}{779} e^{2i(\xi+\eta)} + \frac{152}{2475} e^{2i\eta} + \frac{494}{2001} e^{i(\xi+\eta)},$$

$$\widetilde{P}_9(\xi, \eta) = \frac{19}{15834} - \frac{100}{983} e^{3i(\xi+\eta)} - \frac{19}{15834} e^{3i\xi} + \frac{100}{983} e^{3i\eta},$$

$$\widetilde{P}_{10}(\xi, \eta) = \frac{230}{10131} - \frac{230}{10131} e^{3i\xi}.$$

By Theorem 3.2, we will have 14 tight wavelet frame generators using the constructive steps in [28]. These 14 tight frames ψ^ℓ in terms of Fourier transform can be expressed by

$$(3.11) \qquad \widehat{\psi_8^\ell}(\xi, \eta) = Q^\ell(\xi/2, \eta/2) \, \widehat{\phi_8}(\xi/2, \eta/2), \quad \ell = 1, \ldots, 14,$$

where $Q^\ell(\xi, \eta) = \sum_j \sum_k q_{jk}^{(\ell)} e^{-ij\xi} e^{-ik\eta}$. In the following subsection, we explain how to obtain one low pass and several high pass filters from these ψ_8^ℓ and ϕ_8 and use them for edge detection.

3.3. Image decomposition and reconstruction.
Our edge detector based on box spline frames involves three steps. First, we use the box spline wavelet frame to decompose the input image into many levels of subimages which consist of a low pass part and several high pass parts of the image. Next we set the low pass part to zero and threshold the high pass parts. Finally, we use the resulting high pass parts to get the edge map. The motivation is that edges of an image are represented in high frequencies, while the smoothing parts of an image are represented in terms of translations and dilations of the refinable box spline function. Thus, we set the coefficients of the low pass part in terms of translations and dilations of the box spline to be zero. Meanwhile, since noise is also represented in high frequencies, we apply a percentage thresholding technique (see Algorithm 1) to remove some noise.

Next, we explain how to do image decomposition and reconstruction. For convenience, we use the 14 tight wavelet frame functions $\{\psi^1, \ldots, \psi^{14}\}$, constructed in the previous section based on the box spline function ϕ_8, to illustrate the decomposition and reconstruction. For an image f with finite energy ($f \in L^2(\mathbb{R}^2)$), let $a_{j,\mathbf{k}}$ be the value of the inner product of f with the $\phi_{j,\mathbf{k}}(\cdot) := 2^{2j} \phi_8(2^j \cdot -\mathbf{k})$, i.e., $a_{j,\mathbf{k}} = \langle f, \phi_{j,\mathbf{k}} \rangle$ for $\mathbf{k} \in \mathbb{Z}^2$ and $j \in \mathbb{Z}$. Note that since ϕ_8 is compactly supported and $\int \phi(x)dx = 1$, $a_{j,\mathbf{k}}$ can approximate the grayscale value at $\mathbf{k}$ when j is large enough. Similarly, let $b_{j,\mathbf{k}}^\ell$ be the value of the inner product of f with box spline wavelet framelets $\psi_{j,\mathbf{k}}^\ell(\cdot) := \psi^\ell(2^j \cdot -\mathbf{k})$'s for all $j \in \mathbb{Z}, \mathbf{k} \in \mathbb{Z}^2$, and $\ell = 1, \ldots, 14$, i.e., $b_{j,\mathbf{k}}^\ell = \langle f, \psi_{j,\mathbf{k}}^\ell \rangle$.

Recall that we have

$$\phi_{j,\mathbf{m}}(\cdot) = \sum_{\mathbf{k} \in \mathbb{Z}^2} p_{\mathbf{k}-2\mathbf{m}} \phi_{j+1,\mathbf{k}}(\cdot) \quad \text{and} \quad \psi_{j,\mathbf{m}}^\ell(\cdot) = \sum_{\mathbf{k} \in \mathbb{Z}^2} q_{\mathbf{k}-2\mathbf{m}}^\ell \phi_{j+1,\mathbf{k}}(\cdot)$$

by using the refinable property (3.10) and wavelet frame construction (3.11) for all integers. Note that the refinable function ϕ and tight wavelet frames $\psi^1, \ldots, \psi^{14}$ are locally supported, and the coefficients $\{p_{\mathbf{k}-2\mathbf{m}}\}$ and $\{q_{\mathbf{k}-2\mathbf{m}}^\ell\}$ are finite sequences for all $\ell = 1, \ldots, 14$. Here $p_{\mathbf{k}-2\mathbf{m}}$'s and $q_{\mathbf{k}-2\mathbf{m}}^\ell$'s are associated with the coefficients of the low pass filter P and the high pass filters Q_ℓ, respectively. Due to the limited space in this article, we refer the reader to the webpage http://www.math.uga.edu/~mjlai/boxspline8.html for specific expressions of the low and high pass filters. By taking inner products on both sides of the above two equations with image function f, we obtain the following tight wavelet frame decomposition algorithm:

$$(3.12) \qquad a_{j,\mathbf{m}} = \sum_{\mathbf{k} \in \mathbb{Z}^2} p_{\mathbf{k}-2\mathbf{m}} a_{j+1,\mathbf{k}} \quad \text{and} \quad b_{j,\mathbf{m}}^\ell = \sum_{\mathbf{k} \in \mathbb{Z}^2} q_{\mathbf{k}-2\mathbf{m}}^\ell a_{j+1,\mathbf{k}}$$

for all $j \in \mathbb{Z}, \mathbf{m} \in \mathbb{Z}^2$, and $\ell = 1, \ldots, 14$. Let X_j be the matrix associated with the (j)th level image containing $a_{j,k}$ for all $k \in \mathbb{Z}_+^2$ with $|k| \leq M$ (e.g., M = 512 for a 512 by 512 image), for all $j \in \mathbb{Z}$. Suppose that j is an integer large enough such that the given image f is approximately X_{j+1}, i.e., the pixel value $f_k \approx a_{j+1,k}$. Then the image decomposition procedure is to compute two-dimensional (2D) convolution of P and each $Q_\ell, \ell = 1, \ldots, 14$, with the matrix X_{j+1}; i.e., we find

$$P * X_{j+1}, \quad Q_\ell * X_{j+1}, \quad \ell = 1, \ldots, 14,$$

where $*$ stands for 2D convolution. We then downsample them by deleting all the odd number rows and columns to obtain matrices X_j and $Y_{j,\ell}$ for $\ell = 1, \ldots, 14$.

Next, let us describe the reconstruction procedure. Due to the exact reconstruction, we have

$$(3.13) \qquad \phi_{j+1,\mathbf{m}}(\cdot) = \sum_{\mathbf{k} \in \mathbb{Z}^2} \left\{ p_{\mathbf{m}-2\mathbf{k}} \phi_{j,\mathbf{k}}(\cdot) + \sum_{\ell=1}^{8} q_{\mathbf{m}-2\mathbf{k}}^{\ell} \psi_{j,\mathbf{k}}^{\ell}(\cdot) \right\}$$

by using the perfect condition (3.4). By taking inner products on both sides of the above equation, we have the tight wavelet frame reconstruction algorithm:

$$(3.14) \qquad a_{j+1,\mathbf{m}} = \sum_{\mathbf{k} \in \mathbb{Z}^2} \left\{ p_{\mathbf{m}-2\mathbf{k}} a_{j,\mathbf{k}} + \sum_{\ell=1}^{N} q_{\mathbf{m}-2\mathbf{k}}^{\ell} a_{j,\mathbf{k}}^{\ell} \right\}.$$

Computationally, this can be done by upsampling the image $X_j, Y_{j,\ell}$ by 2, i.e., adding zero columns in between columns of X_j and $Y_{j,\ell}, \ell = 1, \ldots, 14$, then adding zero rows in between rows of the resulting matrices, and then convolving with P and $Q_\ell, \ell = 1, \ldots, 14$.

Usually, X_j, $Y_{j,i}, i = 1, \ldots, \ell$, are called the low pass and high pass parts of the image X_{j+1}, respectively, as they contain the low frequency and high frequency information of X_{j+1}, respectively. If necessary, we can repeat the decomposition process several times by convolving the low pass image X_j with the low pass filter P and the high pass filters Q_ℓ's to get X_{j-1} and $Y_{j-1,\ell}, \ell = 1, \ldots, 14$, respectively. For simplicity, we do one-level decomposition and reconstruction to demonstrate our algorithm.

3.4. Noise removal before edge detection.
Images are usually contaminated by noise. It is sometimes necessary to remove noise from images before computing the edges. A classic method for image denoising is the wavelet shrinkage method, which consists of using a hard or soft thresholding algorithm to trim the wavelet coefficients. In the following, we propose another approach based on the so-called weak orthogonal greedy algorithm (cf. [43]) to further reduce noise.

The main idea is to look for a sparse representation of a noisy image in a redundant wavelet frame system. Let $\Phi = [\phi_1, \ldots, \phi_n]$ ($n = 15$) be a wavelet frame matrix consisting of the values of the framelet functions over discrete grids; i.e., $\phi_1, \ldots, \phi_n$ consist of the values of the refinable functions $\phi(\cdot + (j, k)), \psi^\ell(j, k), \ell = 1, \ldots, 14, (j, k) \in [1, M] \times [1, M]$, for an integer M. Let f be the image, $G_k(f)$ be the kth approximation of f, and $R_k(f)$ be the residual of the kth iteration.

Algorithm 1 (percentage thresholding algorithm). *We begin with* $\Lambda_0 = \emptyset$, $R_0(f) = f$, $G_0(f) = 0$. *Choose a thresholding sequence* $\{t_1, t_2, \ldots\}$ *with all* $t_k \in (0, 1]$.
- *Step 1. For $k \geq 1$, find $M_k = \max_{i \notin \Lambda_{k-1}} |\langle R_{k-1}(f), \phi_i \rangle|$.*
- *Step 2. Let $\Lambda_k = \Lambda_{k-1} \cup \{i, |\langle R_{k-1}(f), \phi_i \rangle| \geq t_k M_k\}$.*
- *Step 3. Let $L_{\Lambda_k}(f)$ be the best approximation (least squares approximation) of $R_{k-1}(f)$ in subspace $S_{\Lambda_k} = span\{\phi_i, i \in \Lambda_k\}$.*
- *Step 4. Update $G_k = G_{k-1}(f) + L_{\Lambda_k}(f)$ and $R_k(f) = R_{k-1}(f) - L_{\Lambda_k}(f)$.*
- *Step 5. If $\|L_{\Lambda_k}(f)\|$ is small enough, stop the algorithm. Otherwise we advance k to $k + 1$ and go to Step 1.*
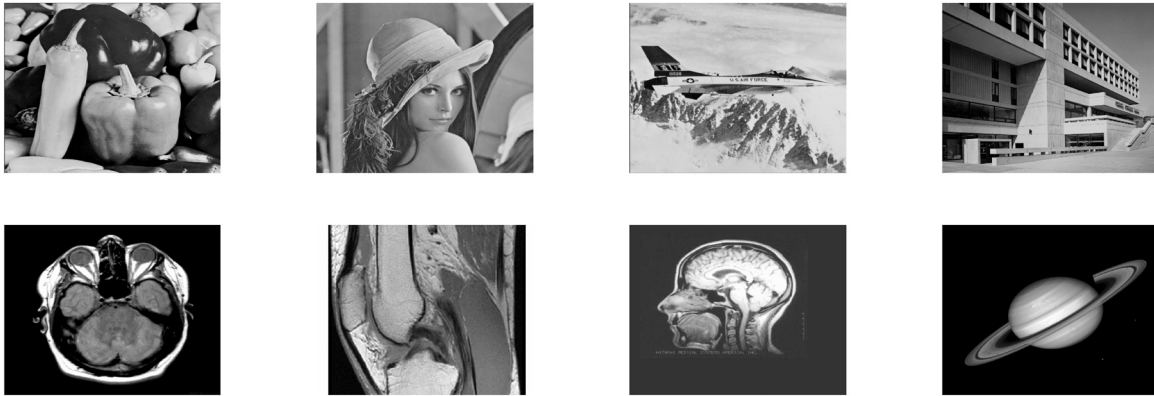
Figure 1. *Eight testing images.*

This algorithm differs from the weak orthogonal greedy algorithm in that in chooses more than one component per iteration. In this paper, we report some numerical results using the wavelet frame based on the tensor product of symmetric quartic B-splines constructed in [8].

In our experiments, we first use the classic hard thresholding method to remove some noise based on wavelet frame decomposition and reconstruction. More specifically, we decompose an image into one low pass part, as well as several high pass parts, and apply the hard thresholding technique to reduce noise from the high pass parts. A smoother image is reconstructed from the low pass part and the resulting high pass parts. Next we use the smoother image as f and the associated tight wavelet frame to form a wavelet frame matrix Φ and then apply Algorithm 1 for further noise reduction. In this experiment, we use a thresholding sequence $\mathbf{t} = \{t_0, t_1, t_2, t_3, \ldots\}$ with $t_i = rt_{i-1}$ with, e.g., $r = 0.78$ and $t_0 = 0.9$ for $i = 1, 2, \ldots, 5$. Although the weak orthogonal greedy algorithm requires $\sum_{i \geq 1} t_i / i = \infty$ to converge, we do only five iterations to reduce noise. Since $\phi_i, i = 1, \ldots, n$, are just various wavelet framelets and their integer translations, the inner products $\langle R_k, \phi_i \rangle$ are just convolutions of ϕ_i with the image or the $(k-1)$th residual. In each iteration of Algorithm 1, we use t_k to form a thresholding $\epsilon_\ell = t_k M_\ell$ with M_ℓ being the largest inner product in absolute value in the ℓth high pass part of the image for $\ell = 1, \ldots, 14$.

The performance of Algorithm 1 is demonstrated using the eight images shown in Figure 1. All images have intensity range $[0, 255]$. We add white Gaussian noise with $\sigma = 20$ to all the images to simulate noisy images. We first apply the hard thresholding method based on the wavelet frame mentioned above to reduce noise and find the best denoised image in terms of the standard peak signal-to-noise ratio (PSNR). Then we use Algorithm 1 to further reduce noise. In the following table, we report the PSNR before and after using Algorithm 1.

Certainly, when using multilevel decomposition and reconstruction of wavelet frames, one may get slightly better PSNR values than those in Table 1. We leave them to interested readers. An advantage of using this approach for image denoising is that one needs only about 25% or fewer nonzero coefficients of a tight wavelet frame to represent a denoised image. In Table 1, we list the percentage of nonzero coefficients (NZC) in a wavelet frame

Table 1
PSNR before and after applying Algorithm 1.

	Peppers	Lena512	F16	Bank
Before	30.25	30.66	30.38	29.47
After	30.37	31.14	30.53	29.53
NZC	15.21%	5.43%	21.67%	27.88%
	Brain	Knee	MRI	Saturn
Before	32.08	30.12	32.48	35.28
After	32.50	30.23	32.80	35.65
NZC	7.62%	23.73%	4.99%	0.523%

representation for each image. Here the NZC is the ratio of the number of nonzero coefficients over the size of images after denoising.

3.5. Image edge detection. We reconstruct the edges of an image based on the zero low pass part and the high pass parts after a percentage thresholding technique which keeps only the lowest 50% largest coefficients. The following is the outline of the image edge detection procedure.

Algorithm 2 (box spline edge detector). *We apply the following steps for an input image f:*

1. *Reduce noise to get a cleaner image $\tilde{f}$ by using Algorithm 1.*
2. *Apply the tight wavelet frame to decompose the image $\tilde{f}$ into one low pass and various high pass subimages.*
3. *Set the low pass part to zero and keep the lowest 50% of the coefficients in absolute value of each of the high pass parts.*
4. *Reconstruct image $\hat{f}$ from the zero low pass and the thresholded high pass components.*
5. *Use k-means classification with two classes to automatically classify $\hat{f}$ into two categories: either 0 or 1.*
6. *Clean up by removing all short isolated edges.*

Comments.

- The only parameter in the proposed Algorithm 2 is the percentage of high pass component coefficients to keep. We understand that fine tuning of this threshold might lead to better results, but to make it simple, we just use 50%. It turns out that the numerical results are consistently satisfactory already. Moreover, the last step in Algorithm 2 is also applied to other edge detectors.
- Note that noise exists in both high frequency and low frequency parts. Although cutting off a portion of the high frequency part as we do in the third step of the above edge detection algorithm does remove some high frequency noise, there is still some left. To avoid false edges and other artifacts due to noise, we apply Algorithm 1 to reduce noise before detecting edges. This denoising procedure, however, makes the overall edge detection approach scale variant.
- The k-means classification in the fifth step of the algorithm is to automatically obtain a binary edge map from the result of the fourth step of Algorithm 2. It does not help with detecting edges or fine features more accurately.

4. Numerical experiments. This section consists of three sets of experimental results. In subsection 4.1, we compare the proposed box spline edge detector with some selected edge detectors: Prewitt, Canny, Chan–Vese, wavelet [31], and shearlet [46]. In subsection 4.2, we test the performance of the proposed method on detecting edges of noisy images. Subsections 4.3 and 4.4 focus on detecting Dirac and hidden edges, respectively. The last subsection discusses the application of the box spline based edge detector on object identification.

4.1. Comparison of several edge detection methods. We demonstrate the advantage of the proposed box spline edge detection method through comparing it with some methods mentioned in section 2. While there have been attempts to propose quantitative measures for the performance of an edge detector, there seems to be no consensus on which one is the best. We select two popular measures: Pratt's figure of merit (FOM) [37] and probability of detection (P_D) [1], the probability of an edge detector finding true edges. Computation of both of these measures requires ground truth edges. Thus, we create one image with ground truth edges outlined by hand (Figure 2).

Pratt's figure of merit is a measure describing the distance from the detected edges to the ground truth edges. It is defined as

$$FOM = \frac{1}{\max(n_d, n_g)} \sum_{k=1}^{n_g} \frac{1}{1 + \alpha d(k)},$$

where n_d, n_g are the number of points on the detected and ground truth edges, respectively, $d(k)$ is the distance from the kth detected edge point to the actual ground truth edges, and α is a scaling constant that we set as $1/9$. The larger figure of merit the better.

Edge detection can also be cast as a hypothesis testing problem that determines if an image pixel is on edge or not. The efficiency of edge detection can thus be evaluated using a metric from statistics: the probability of correct edge detection P_D. It measures the ability of an edge detection method in correctly locating actual edges. Let M_d, M_g be the detected and the ground truth binary edge maps with 1,0 intensity representing edge and nonedge, respectively. Then P_D is defined as

$$P_D = \text{Prob}(M_d = 1 | M_g = 1) = \frac{\text{Prob}(M_d = 1, M_g = 1)}{\text{Prob}(M_g = 1)}.$$

To avoid the intervention of the denoising process on the performance evaluation of edge detection methods, we start with a simulated clean image (shown in Figure 2(a)) with ground truth edges (Figure 2(b)). It contains objects of various shapes and rectangular boxes with gradually changing intensities. We apply Prewitt, Chan–Vese, wavelet, and box spline edge detection methods (a) under each method's best parameter setting and to obtain results as shown in (c)–(f). It can be seen that the box spline result has the highest figure of merit and is also visually the closest to the ground truth edges.

Results in Figure 2 are computed using each method's best possible parameter selection. Note that more horizontal lines on the left can be detected by lowering the threshold value, but due to the fact that those areas have low intensities and low contrast, one has to set the threshold extremely low to detect those horizontal lines. As a result, we pay the price of having
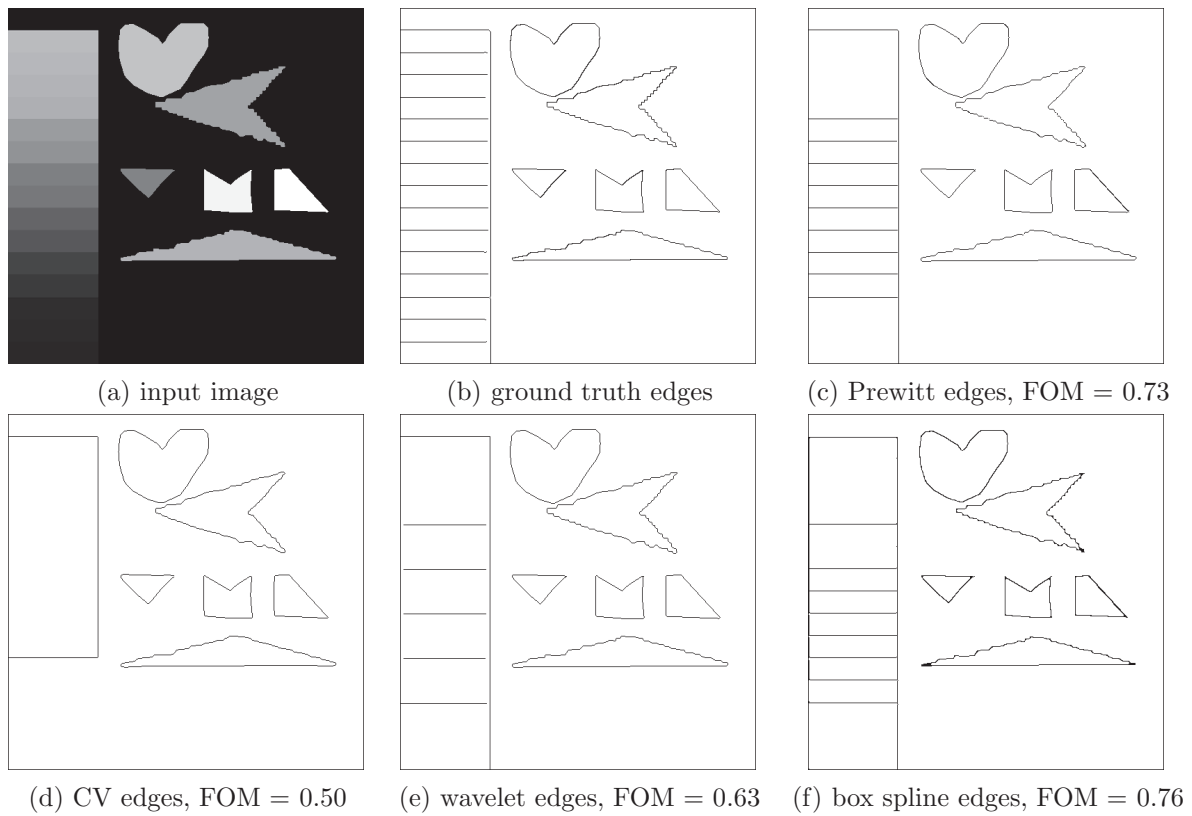
(a) input image   (b) ground truth edges   (c) Prewitt edges, FOM = 0.73

(d) CV edges, FOM = 0.50   (e) wavelet edges, FOM = 0.63   (f) box spline edges, FOM = 0.76

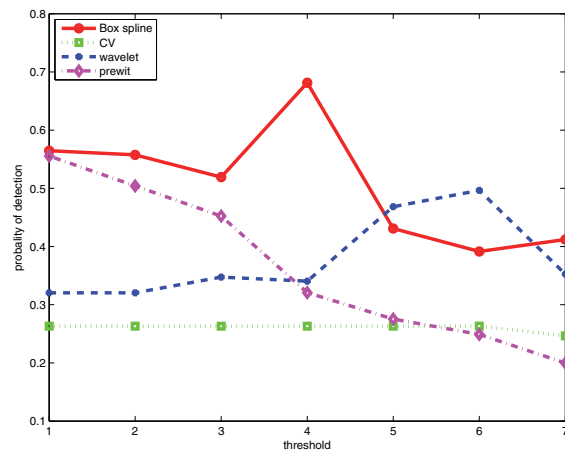**Figure 2.** *Comparison of four edge detectors on a synthetic image.*

Figure 3. *Compare probability of detection of the four edge detectors on various parameters. The test image is the one shown in Figure 2(a).*
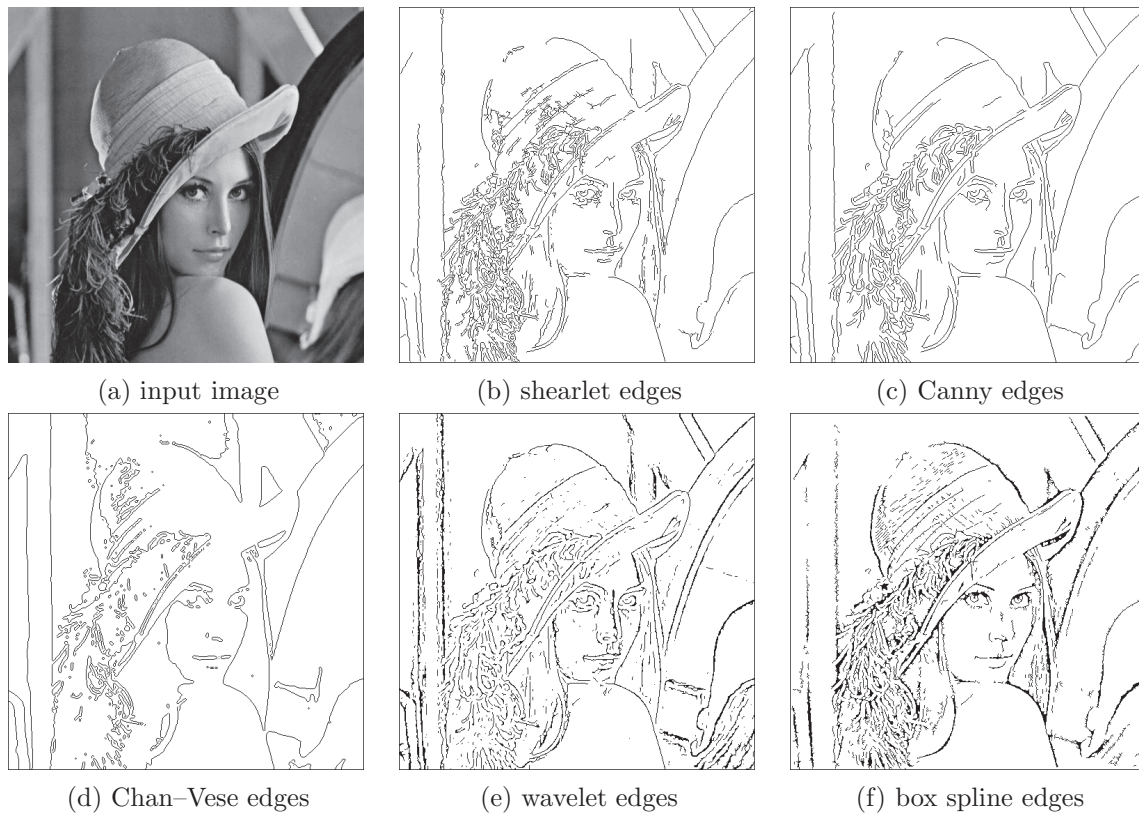
(a) input image   (b) shearlet edges   (c) Canny edges

(d) Chan–Vese edges   (e) wavelet edges   (f) box spline edges

Figure 4. *Comparison of five edge detectors on Lena image.*

broken and/or nonsmooth edges almost everywhere at the geometries on the right-hand side. We thus present the results that have the best overall appearance. In practice and in general, one most likely just chooses an ad hoc parameter. In Figure 3, we compare P_D of the four edge detection methods under seven different ad hoc parameters. One can see that the box spline edge detection method has significantly higher P_D than the other four methods except for two out of seven of the wavelet edge detection results.

Next, we compare those edge detectors on natural images with more details (Figures 4–9). No ground truth edges are available for quantitative comparison, but visual comparison shows that the box spline method performs better in catching fine edges. See, for instance, the edges of Lena's hair and eyes in Figure 5 and those of the table cloth, pants, and face in Figure 7, as well as the edges of the textures and plants in Figure 9.

From a computation time perspective, the proposed algorithm is indeed slower than Canny and Prewitt algorithms. Canny and Prewitt use two convolutions (x-direction and y-direction), while our algorithm uses 15 convolutions with one low pass and 14 high pass box spline filters. The sizes of our filters are also bigger. The current nonoptimized implementation of the proposed algorithm is about eight times as expensive as that of the Canny and Prewitt algorithms on average. It is about eight times and five times as expensive as that of the wavelet and shearlet based methods, respectively. However, it is comparable to that of
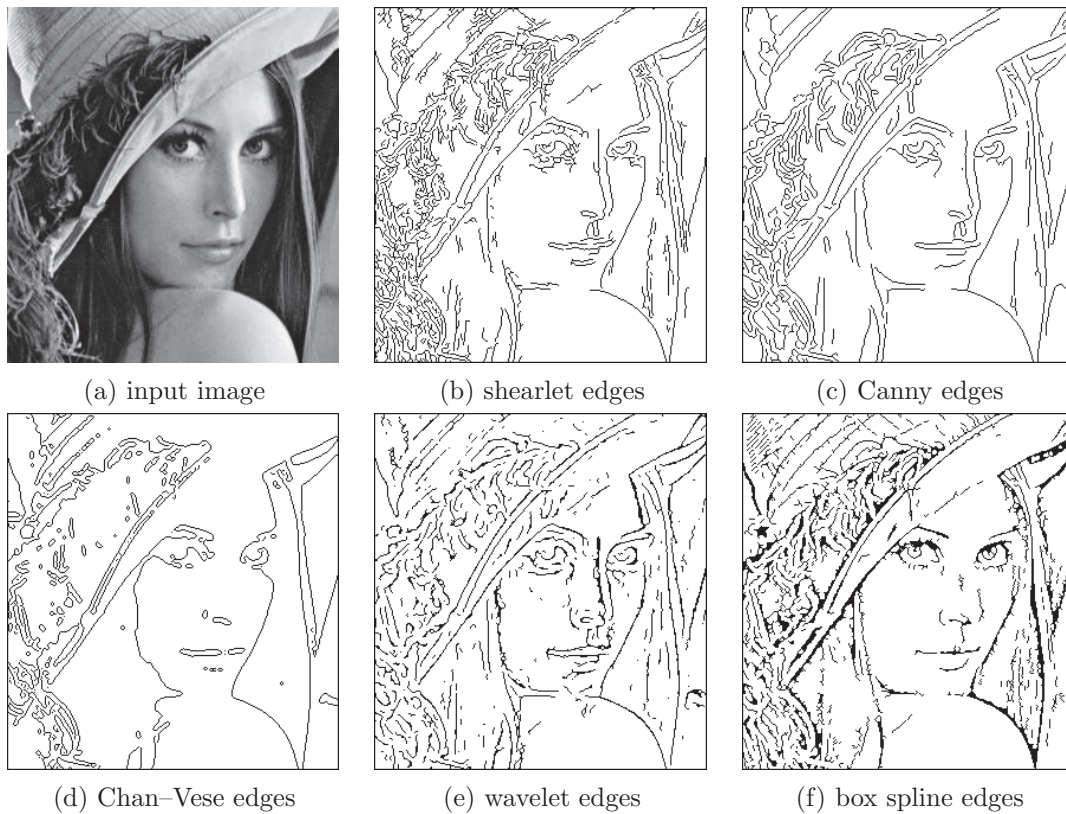
(a) input image   (b) shearlet edges   (c) Canny edges

(d) Chan–Vese edges   (e) wavelet edges   (f) box spline edges

Figure 5. *Zoom-in comparison of five edge detectors on the Lena image shown in Figure* 4.

the Chan–Vese method.

Note that the wavelet [31] and shearlet [46] methods detect edges by analyzing the change of the transform coefficients across different scales. They are very different from the proposed edge detector based on low and high pass filters designed using box spline frames. One can also use the low and high pass filters in discrete wavelets such as Haar, D4, D6, and biorthogonal 9/7 in the proposed edge detector scheme to compute edges. We did the experiments, but the performance is not comparable. We have also inserted discrete shearlet kernels from the fast finite shearlet transform (FFST) toolbox [18] into the proposed edge detection, but the results are not as good as those in [46]. We thus do not include them here.

4.2. Edge detection for noisy images. We also test the performance of the proposed edge detection method on various noisy images. Next, in Figure 10, we show the robustness of the proposed edge detector to noise by exhibiting edges detected from noisy images with SNR as low as 9. White Gaussian noise with standard deviation $\sigma = 40$ is added to each of the three clean images with intensity in $[0, 255]$. For each of the noisy images, we apply a standard wavelet frame denoising method (hard thresholding) to obtain a cleaner image which is fed into Algorithm 1 for further denoising if necessary. We then apply Algorithm 2 on the denoised image to detect edges.

One can see that most of the edges/features are still detected correctly. However, we do
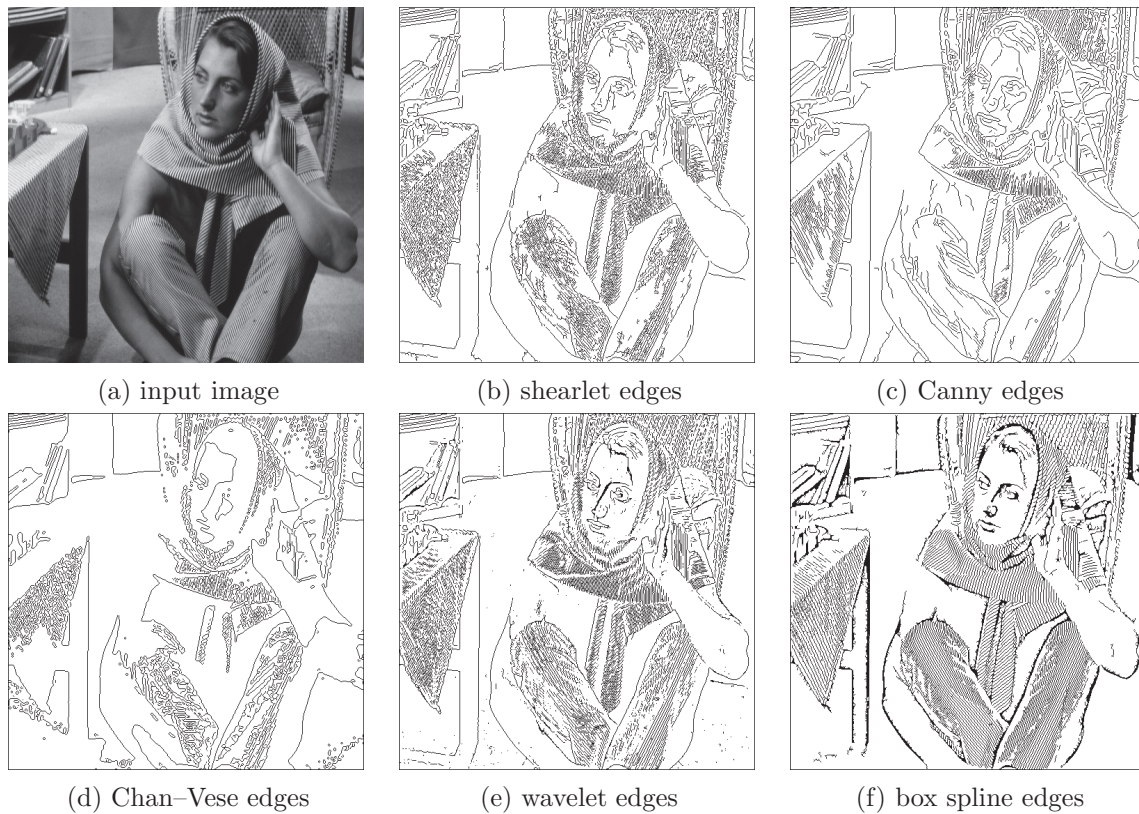
(a) input image	(b) shearlet edges	(c) Canny edges
(d) Chan–Vese edges	(e) wavelet edges	(f) box spline edges

Figure 6. *Comparison of five edge detectors on Barbara image.*

see some artifacts and lost edges due to the deterioration of the input images.

4.3. Dirac edges. It is well known that the gradient based edge detectors such as Canny and Prewitt fail to detect Dirac edges (locations with momentary intensity changes) accurately. They mistakenly treat locations to the left and right sides of Dirac edges as a discontinuity in intensity and thus detect double step edges instead of Dirac edges. Our box spline wavelet frame detector can find such Dirac edges exactly. We show one example here. The left panel of Figure 11 is a testing image. Our box spline edge detector finds that the exact edges appear exactly the same as the left panel of Figure 11.

4.4. Application to hidden edge detection. We now apply the box spline wavelet frame edge detector to find hidden edges, i.e., locations with some kind of discontinuous derivatives of image intensity. Detecting such edges has important applications—for instance, aircraft surface manufacturing. To reduce the turbulence, the surface of the body of an aircraft needs to be C^2 smooth to avoid generating singularities of airflows. One way to find defects in the surface of an aircraft body is to find locations with discontinuous first- or second-order derivatives, i.e., hidden edges. In this subsection, we artificially create a surface with
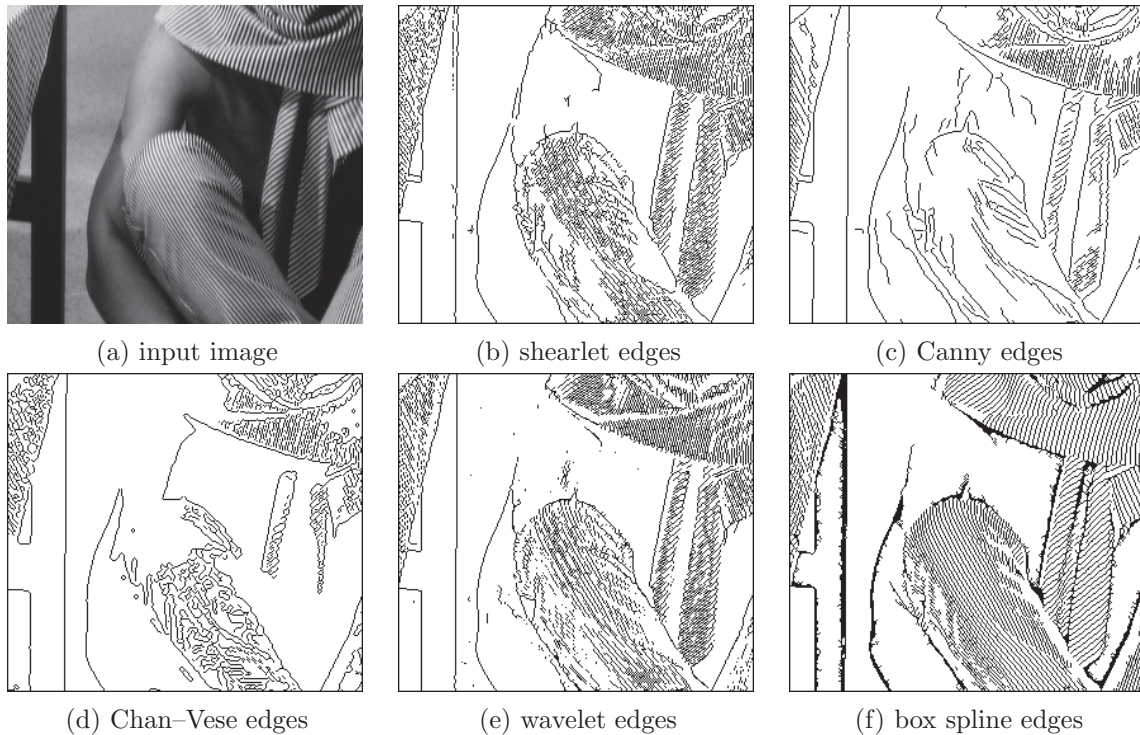
(a) input image

(b) shearlet edges

(c) Canny edges

(d) Chan–Vese edges

(e) wavelet edges

(f) box spline edges

Figure 7. *Zoom-in comparison of five edge detectors on the Barbara image shown in Figure* 6.

discontinuous first-order derivatives. For example,

$$z_1(x,y) = \begin{cases} (x-1)^2 + (y-1)^2 - 0.5 & \text{if } (x-1)^2 + (y-1)^2 > 0.5, \\ 0 & \text{otherwise} \end{cases}$$

over $(x,y) \in [0, 2.55]^2$. The three-dimensional (3D) graph and the 2D intensity image of the function $z_1(x,y)$ are shown in the left and the right panels of Figure 12, respectively.

From the 2D intensity image, we hardly see any edges. However, from the 3D surface, we can easily see the places where the first-order derivatives are discontinuous. As another example, let

$$z_2(x,y) = \begin{cases} (x+y-1.5)^2 - 0.5 & \text{if } (x+y-1.5)^2 > 0.5, \\ 0 & \text{otherwise} \end{cases}$$

over $(x,y) \in [0, 2.55]^2$. The graph and the image of the function $z_2(x,y)$ are shown in Figure 13. Hidden edges are displayed in Figure 14.

We next present an example to detect hidden edges with discontinuous second-order derivatives. The synthetic example is as follows:

$$z_3(x,y) = \begin{cases} ((x-1)^2 + (y-1)^2 - 0.35)^2 & \text{if } (x-1)^2 + (y-1)^2 \geq 0.35, \\ 0.125 - ((x-1.05)^2 + (y-1)^2)^2 & \text{if } ((x-1.05)^2 + (y-1)^2)^2 \leq 0.125, \\ 0 & \text{otherwise} \end{cases}$$

| (a) input image | (b) shearlet edges | (c) Canny edges |

| (d) Chan–Vese edges | (e) wavelet edges | (f) box spline edges |
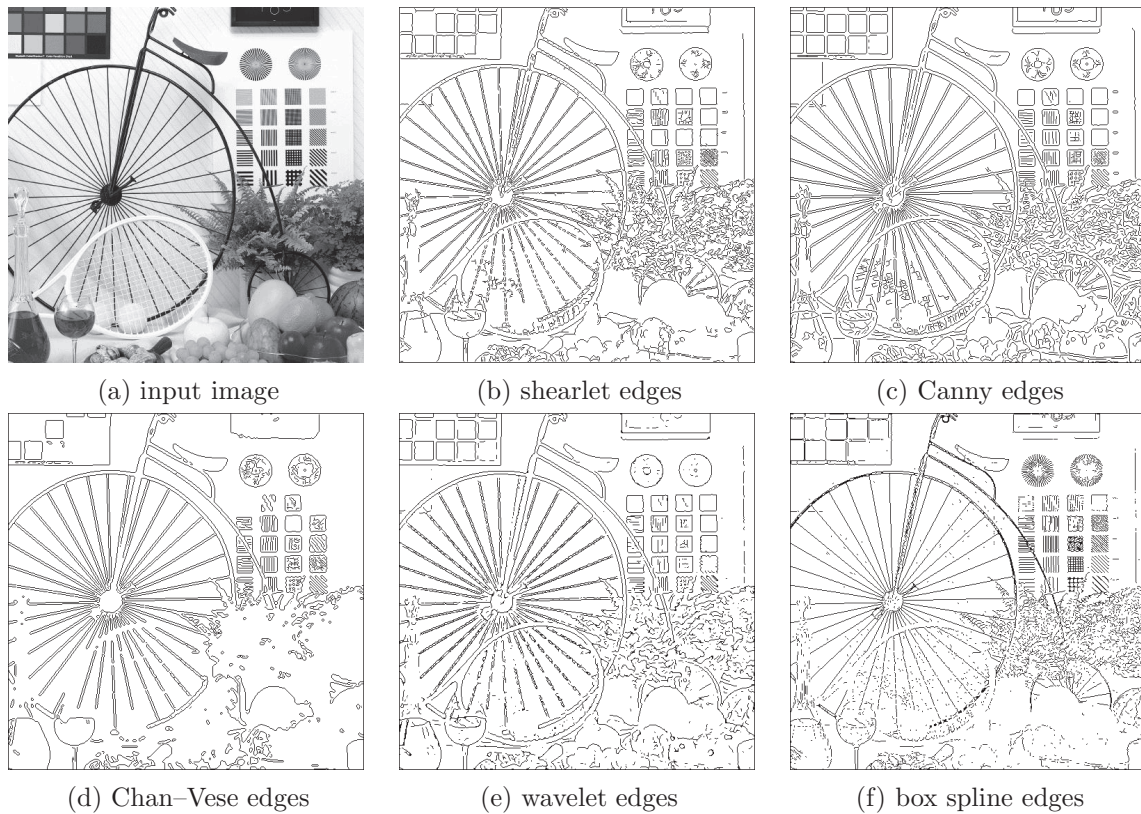
Figure 8. *Comparison of five edge detectors on a bike image.*

over $(x, y) \in [0, 2.55]^2$. The graph and the image of the function $z_3(x, y)$ are shown in Figure 15, from which we can hardly see by the naked eye any irregularities or defects of the surface. However, our edge detector reveals hidden edges where possible defects may be located (Figure 16).

4.5. Application to object identification. The results of the box spline edge detector can be used for feature extraction, object identification, region segmentation, etc. In this subsection, we provide one example of a practical application: to segment objects of interest from medical images.

As shown in Figure 17, starting with an 8-bit grayscale (valued in between 0 and 255) cardiac image (top left), we first use the proposed box spline edge detector to create a 1-bit (valued 0 or 1) edge mask (top right), followed by a clean-up process to remove isolated edges (bottom left). To get the two objects of interest in the center of the image, we drop a small box inside each of the two objects and grow the regions [45] until they touch the borders of the objects. The results are shown in the bottom right panel. Applying region growing segmentation to the 1-bit 0-1 edge mask is better than applying it to the 8-bit gray scale image as borders of the objects of interest are more reliable and ready to be used in the 1-bit edge map. One may calculate the areas of the regions of interest for medical image analysis purposes afterward.
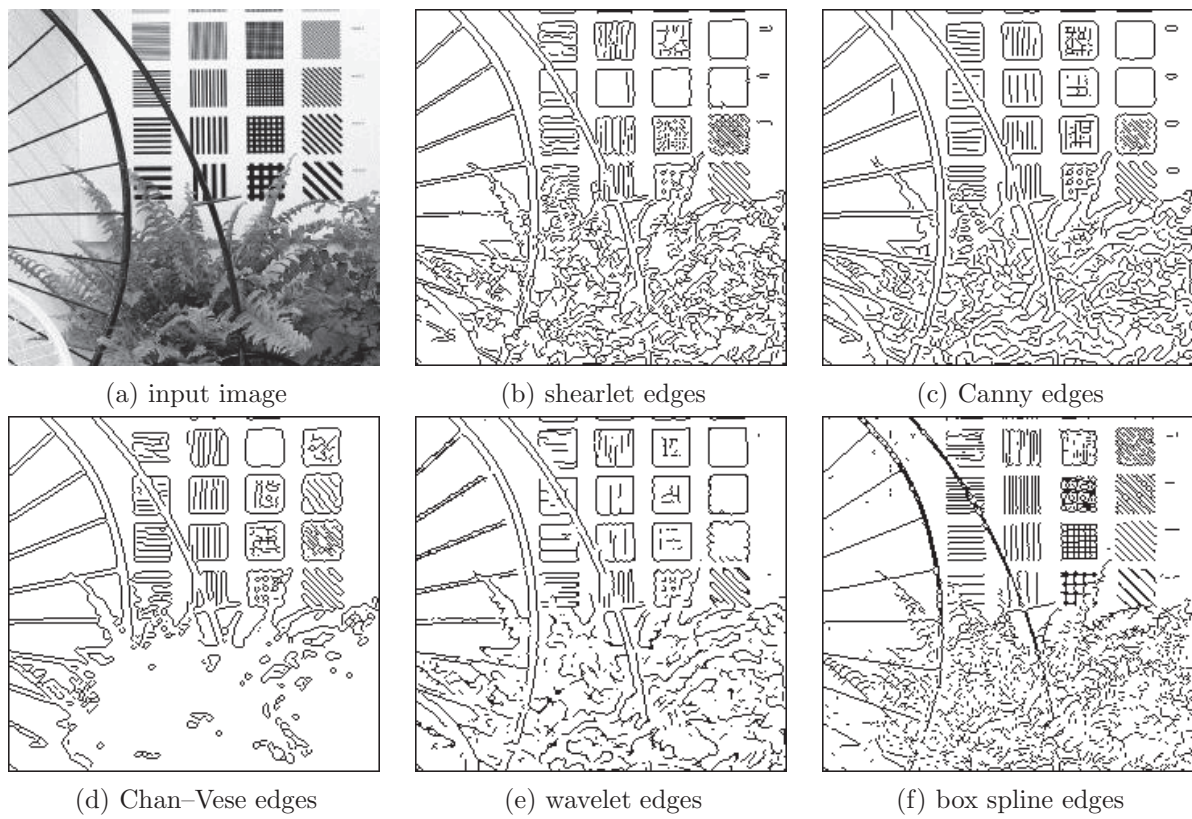
(a) input image   (b) shearlet edges   (c) Canny edges

(d) Chan–Vese edges   (e) wavelet edges   (f) box spline edges

Figure 9. *Zoom-in comparison of five edge detectors on the bike image shown in Figure* 8.
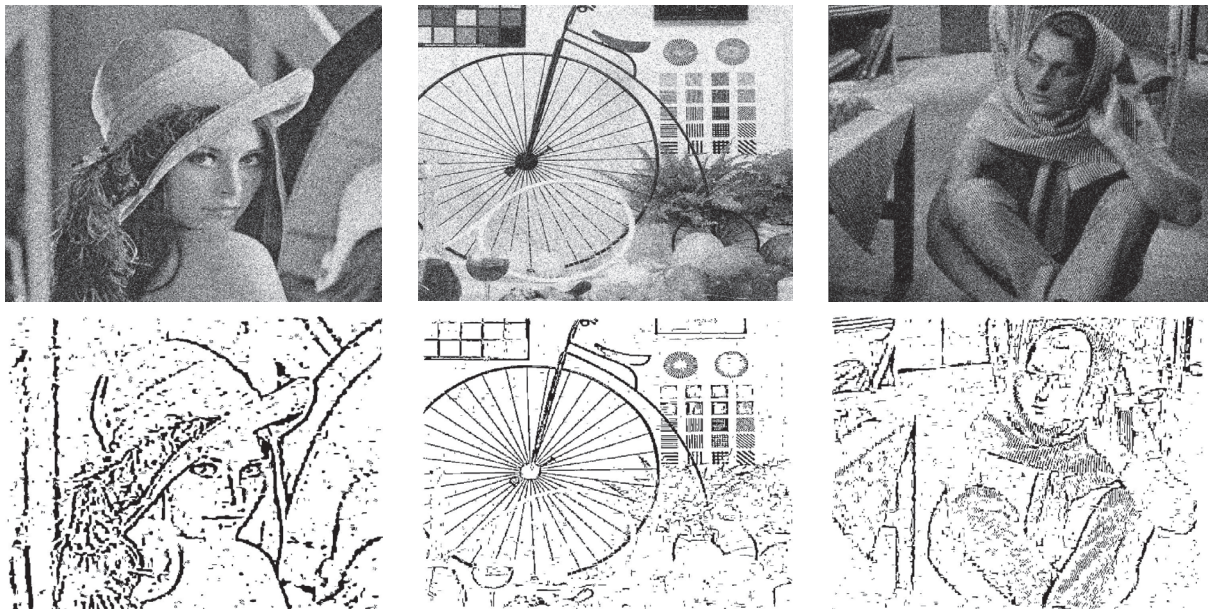

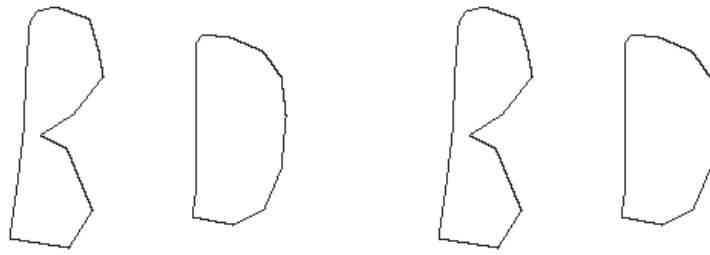**Figure 10.** *Edges (second row) detected from noisy images (first row).*

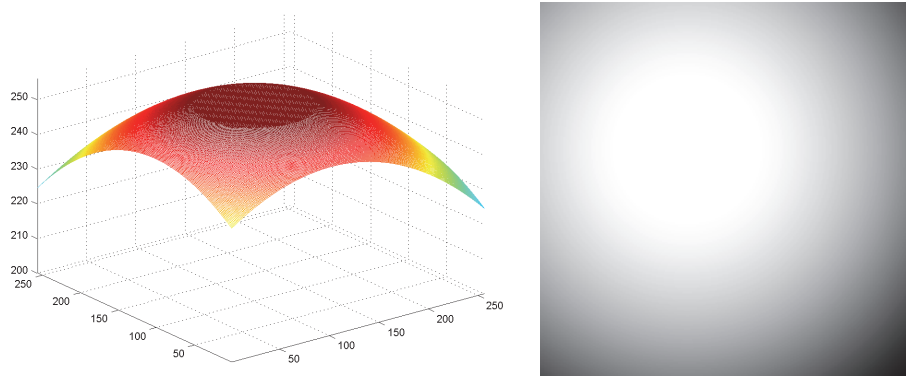**Figure 11.** *The proposed box spline edge detector is able to detect Dirac edges.*

Figure 12. *The graph (left) and the image (right) of function z_1 with discontinuous derivatives around a circle.*

Figure 13. *The graph (left) and the image (right) of function z_2 with discontinuous derivatives at two lines.*
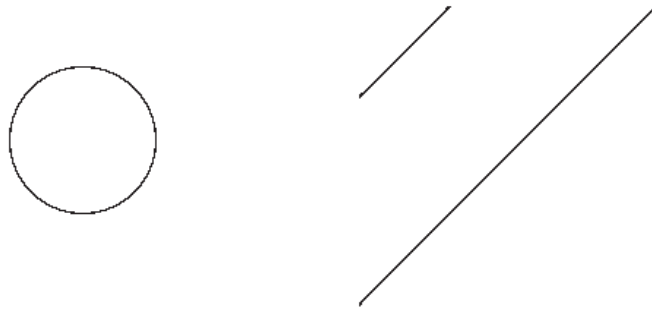
Figure 14. *Locations of hidden edges of the images in Figures* 12 *(left) and* 13 *(right).*
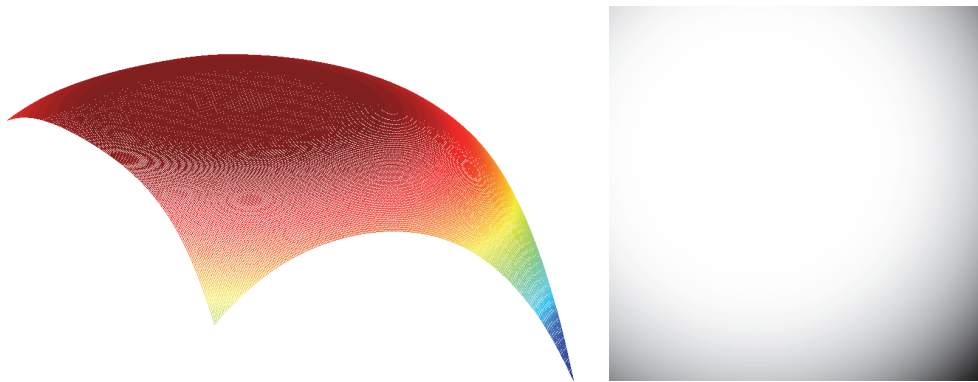
Figure 15. *The graph (left) and the image (right) of function* z_3 *with discontinuous derivatives at two circles.*
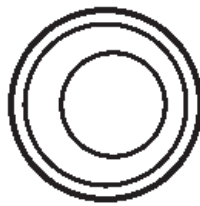
Figure 16. *Hidden edges found from the image in Figure* 15 *using the proposed box spline edge detector.*
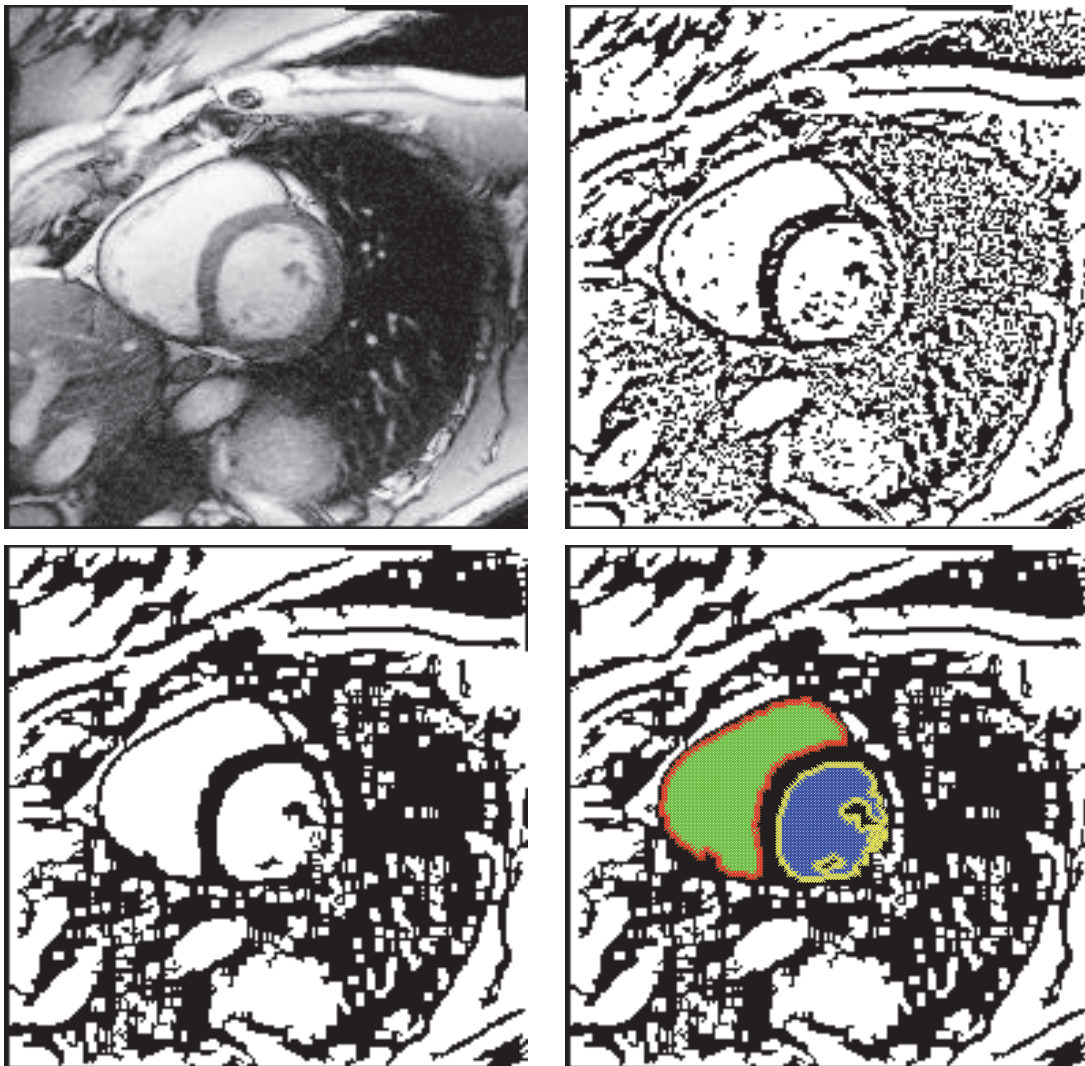
Figure 17. *A medical image (top left), the resulting image based on box spline tight wavelet frame detector (top right), cleaner edges (bottom left), and the outline of two regions of interest (bottom right).*

5. Conclusions. We present an edge detection algorithm based on a new eight direction box spline tight frame constructed using the theory in [28]. The construction of tight wavelet frames based on this eight direction box spline is nontrivial as there is no theory to guarantee the existence of a solution to the polynomial equation (3.7). Also, how to find a solution for a general polynomial equation (3.7) is still open. We use a brute force method to solve it. Once the framelets are found, computing edges based on these framelets is very simple and does not need complicated optimization criteria. It applies box spline based wavelet transforms to decompose a given image into one low pass and several high pass components. When there is no noise, edges are only the inverse wavelet transform of the high pass components. When noise exists, one needs some thresholds to separate true edges from noises, both of which

belong to high pass components. Quantitative and qualitative comparisons with several other existing edge detectors demonstrate the effectiveness and efficiency of the proposed method in detecting step edges. Our edge detector is also able to detect Dirac edges and hidden edges. In addition, we show that the proposed method is robust to noise. Finally, we apply the edge detector to object identification.

REFERENCES

[1] K. E. ABDOU AND K. K. PRATT, *Quantitative design and evaluation of enhancement/thresholding edge detectors*, Proc. IEEE, 67 (1979), pp. 753–763.

[2] L. AMBROSIO AND V. M. TORTORELLI, *On the approximation of free discontinuity problems*, Boll. Un. Mat. Ital. B (7), 6 (1992), pp. 105–123.

[3] J. CANNY, *A computational approach to edge detection*, IEEE Trans. Pattern Anal. Mach. Intell., 8 (1986), pp. 679–714.

[4] T. F. CHAN AND L. A. VESE, *Active contours without edges*, IEEE Trans. Image Process., 10 (2001), pp. 266–277.

[5] M. CHRINA, M. PUTINAR, C. SCHEIDERER, AND J. STÖCKLER, *An algebraic perspective on multivariate tight wavelet frames*, Constr. Approx., to appear.

[6] M. CHRINA AND J. STÖCKLER, *Construction of tight wavelet frames by semi–definite programming*, J. Approx. Theory, 162 (2010), pp. 1429–1449.

[7] C. K. CHUI, *Multivariate Splines*, CBMS-NSF Regional Conf. Ser. in Appl. Math. 54, SIAM, Philadelphia, 1988.

[8] C. K. CHUI AND W. HE, *Compactly supported tight frames associated with refinable functions*, Appl. Comput. Harmon. Anal., 8 (2000), pp. 293–319.

[9] C. K. CHUI AND W. HE, *Construction of multivariate tight frames via Kronecker products*, Appl. Comput. Harmon. Anal., 11 (2001), pp. 305–312.

[10] C. K. CHUI, W. HE, AND J. STÖCKLER, *Compactly supported tight and sibling frames with maximum vanishing moments*, Appl. Comput. Harmon. Anal., 13 (2002), pp. 224–262.

[11] I. DAUBECHIES, *Ten Lectures on Wavelets*, CBMS-NSF Regional Conf. Ser. in Appl. Math. 61, SIAM, Philadelphia, 1992.

[12] I. DAUBECHIES, B. HAN, A. RON, AND Z. SHEN, *Framelets: MRA-based constructions of wavelet frames*, Appl. Comput. Harmon. Anal., 14 (2003), pp. 1–46.

[13] C. DE BOOR, K. HÖLIG, AND S. RIEMEMSCHNEIDER, *Box Splines*, Springer-Verlag, New York, 2003.

[14] R. DERICHE, *Fast algorithms for low-level vision*, IEEE Trans. Pattern Anal. Mach. Intell., 12(A) (1990), pp. 78–87.

[15] G. EASLEY, D. LABATE, AND W. Q. LIM, *Sparse directional image representations using the discrete shearlet transform*, Appl. Comput. Harmon. Anal., 25 (2008), pp. 25–46.

[16] J. GERONIMO AND M. J. LAI, *Factorization of multivariate positive Laurent polynomials*, J. Approx. Theory, 139 (2006), pp. 327–345.

[17] W. GUO AND F. HUANG, *A local mutual information guided denoising technique and its application to self-calibrated partially parallel imaging*, in MICCAI, Part II, Lecture Notes in Comput. Sci. 5242, Springer, Berlin, 2008, pp. 939–947.

[18] S. HÄUSER, *Fast finite shearlet transform*, http://arxiv.org/abs/1202.1773v1, 2012.

[19] W. He and M. J. Lai, *Construction of bivariate compactly supported biorthogonal box spline wavelets with arbitrarily high regularities*, Appl. Comput. Harmon. Anal., 6 (1999), pp. 53–74.

[20] B. Jähne, H. Scharr, and S. Korgel, *Principles of filter design*, in Computer Vision and Applications, Vol. 2, Signal Processing and Pattern Recognition, B. Jähne, H. Haußecker, and P. Geißler, eds., Academic Press, San Diego, CA, 1999, pp. 125–151.

[21] J. J. Koenderink and A. J. van Doom, *Generic neighborhood operators*, IEEE Trans. Pattern Anal. Mach. Intell., 14(F) (1992), pp. 597–605.

[22] D. Labate, W.-Q. Lim, G. Kutyniok, and G. Weiss, *Sparse multidimensional representation using shearlets*, in Wavelets XI, Proc. SPIE 5914, SPIE, Bellingham, WA, 2005, pp. 254–262.

[23] M. J. Lai, *Fortran subroutines for B-nets of box splines on three- and four-directional meshes*, Numer. Algorithms, 2 (1992), pp. 33–38.

[24] M. J. Lai, *Construction of multivariate compactly supported prewavelets in l_2 spaces and pre-Riesz basis in Sobolev spaces*, J. Approx. Theory, 142 (2006), pp. 83–115.

[25] M. J. Lai and K. Nam, *On the number of tight wavelet framelets associated with multivariate box splines*, J. Approx. Theory Appl., to appear.

[26] M. J. Lai and A. Petukhov, *Method of virtual components in the multivariate setting*, J. Fourier Anal. Appl., 16 (2010), pp. 471–494.

[27] M. J. Lai and L. L. Schumaker, *Spline Functions over Triangulations*, Cambridge University Press, Cambridge, UK, 2007.

[28] M.-J. Lai and J. Stöckler, *Construction of multivariate compactly supported tight wavelet frames*, Appl. Comput. Harmon. Anal., 21 (2006), pp. 324–348.

[29] S. Lanser and W. Eckstein, *Eine modification des deriche-verfahrens zur kantendetektion*, in Mustererkennung 1991, Informatik Fachberichte, DAGM Symposium, Vol. 290, B. Radig, ed., Springer, Berlin, 1991, pp. 151–158.

[30] S. Mahmoodi, *Edge detection filter based on Mumford–Shah Green function*, SIAM J. Imaging Sci., 5 (2012), pp. 343–365.

[31] S. Mallat and S. Zhong, *Characterization of signals from multiscale edges*, IEEE. Trans. Pattern Anal. Mach. Intell., 14 (1992), pp. 710–732.

[32] D. Marr and E. Hildreth, *Theory of edge detection*, Proc. Roy. Soc. London Ser. B, 207 (1980), pp. 187–217.

[33] D. Mumford and J. Shah, *Optimal approximation by piecewise smooth functions and associated variational problems*, Comm. Pure Appl. Math., 42 (1989), pp. 557–685.

[34] K. Nam, *Tight Frame Construction and Its Application for Image Processing*, Ph.D. thesis, University of Georgia, Athens, GA, 2005.

[35] S. Osher and J. A. Sethian, *Fronts propagating with curvature-dependent speed: Algorithms based on Hamilton-Jacobi formulations*, J. Comput. Phys., 79 (1988), pp. 12–49.

[36] I. Pitas and A. N. Venetsanopoulos, *Nonlinear Digital Filters: Principles and Applications*, Kluwer Academic Publishers, Dordrecht, The Netherlands, 1990.

[37] W. K. Pratt, *Digital Image Processing*, Wiley-Interscience, New York, 1978.

[38] D. Qi, F. Guo, and L. Yu, *Medical image edge detection based on omnidirectional multi-scale structure element of mathematical morphology*, in Proceedings of the IEEE International Conference on Automation and Logistics, IEEE, Washington, DC, 2007, pp. 2281–2286.

[39] A. Ron and Z. Shen, *Compactly supported tight affine spline frames in $L_2(\mathbf{R}^d)$*, Math. Comp., 67 (1998), pp. 191–207.

[40] A. Ron and Z. Shen, *Construction of compactly supported affine frames in $L_2(R^d)$*, in Advances in Wavelets, Springer, New York, 1998, pp. 27–49.

[41] J. Serra, *Image Analysis and Mathematical Morphology*, Academic Press, New York, 1982.

[42] W. Stefan, R. A. Renaut, and A. Gelb, *Improved total variation-type regularization using higher-order edge detectors*, SIAM J. Imaging Sci., 3 (2010), pp. 232–251.

[43] V. N. Temlyakov, *Greedy approximation*, Acta Numer., 17 (2008), pp. 235–409.

[44] B. Tian, H. Yuan, and X. Yue, *Feature extraction algorithm for space targets based on fractal theory*, in Proceedings of the Second International Conference on Space Information Technology, SPIE Proc. 6795, SPIE, Bellingham, WA, 2007, 679518.

[45] S. Umbaugh, *Computer Vision and Image Processing: A Practical Approach Using CVIPtools*, Prentice–Hall, Englewood Cliffs, NJ, 1997.

[46] S. Yi, D. Labate, R. G. Easley, and H. Krim, *A shearlet approach to edge analysis and detection*, IEEE Trans. Image Process., 18 (2009), pp. 929–941.

[47] L. Zhai, S. Dong, and H. Ma, *Recent methods and applications on image edge detection*, in Proceedings of the International Workshop on Geoscience and Remote Sensing, Shanghai, China, 2008, pp. 332–335.

[48] L. Zhang, A. Butler, and C. Sun, *Fractal dimension assessment of brain white matter structural complexity post stroke in relation to upper-extremity motor function*, Brain Research, 1228 (2008), pp. 229–240.

[49] D. Ziou and S. Tabbone, *Edge detection techniques—an overview*, Internat. J. Pattern Recognition Image Anal., 8 (1998), pp. 537–559.